applied optics

Noise analysis of the Vernier anode

Airong Zhao,[1,2] Qiliang Ni,[1,*] and Weixing Yu[3]

[1]Changchun Institute of Optics, Fine Mechanics and Physics, Chinese Academy of Sciences, Changchun 130033, China
[2]University of Chinese Academy of Sciences, Beijing 10039, China
[3]Shenzhen University, Shenzhen 518061, China
*Corresponding author: niqiliang@hotmail.com

Received 13 April 2015; revised 24 June 2015; accepted 24 June 2015; posted 24 June 2015 (Doc. ID 237946); published 30 July 2015

In this work, the partition noise and the electronic noise of the Vernier anode are thoroughly analyzed based on the theory of statistical variation and error analysis. A new method calculating the inter-electrode capacitance of the Vernier anode is proposed, and the electronic noise's effect is discussed in detail, which is useful for the optimal design of a Vernier anode in the induced charge mode. The calculated results of the inter-electrode capacitance for a 0.891 mm period Vernier anode are in good agreement with the measured results.

OCIS codes: (040.7480) X-rays, soft x-rays, extreme ultraviolet (EUV); (040.5160) Photodetectors; (110.4280) Noise in imaging systems.

http://dx.doi.org/10.1364/AO.54.006904

1. INTRODUCTION

Photon-counting imaging detectors with a microchannel plate (MCP) and a position-sensitive anode have been widely used in low-light-level image fields such as UV astronomy [1] and far-UV ionosphere remote sensing [2] due to their capability of detecting an extremely faint light signal. These detectors employ photocathodes and MCPs to convert a photon into a charge cloud. The charge cloud's centroid position, which corresponds to the coordinates of the incident event position, can be measured by the readout electronics. The position-sensitive anodes can be classified into two kinds: one is the discrete anode [3], which identifies the event position digitally with a high count rate but with a low spatial resolution, and the other is the continuous anode [4,5], which gets the event position in analog mean with a high spatial resolution. The charge divided anode, as a kind of continuous anode, though, is rate-limited compared with highly parallel systems, but can achieve a very high position resolution [6,7].

The Vernier anode, as a kind of charge divided anode, has been proved to be able to achieve a spatial resolution of better than 0.01 mm in the induced charge mode [8]. It is well known that the spatial resolution of the charge divided anode is totally determined by its partition noise and electronic noise [9,10]. The partition noise is caused by the statistical variation of the charge cloud due to the divided electrodes and therefore is related to the anode's structure and the charge cloud's distribution. The electronic noise arises due to the charge sensitive amplifier (CSA), which influences the measurement of the signal and hence the event position. It is related to the capacitive load, which corresponds to the inter-electrode capacitances [9] of the anode. There have been numerous publications to discuss the noises [10,11] and the capacitance of the WSA [9,12,13]. However, so far there has been no public report to discuss the noise and the inter-electrode capacitance of the Vernier anode. In addition, all previous work regarding the inter-electrode capacitances [12] only discusses the case in which the electrode strips have the same width, which leads to inaccuracy in calculating the inter-electrode capacitance.

In this work, the partition noise and the electronic noise of the Vernier anode are derived in theory, and the optimal charge cloud's width is proposed by simulating the effect of the charge cloud width on the decode algorithm. At the same time, an approach is proposed to calculate the inter-electrode capacitance of the anode. The results are helpful for those who want to design a Vernier anode with high spatial resolution.

2. PARTITION NOISE OF THE VERNIER ANODE

Figure 1 shows the structure of a Vernier anode with nine electrodes that constitute two pitches on a plane. A pitch is grouped into three triplets, A, B, and C. Each triplet with the same width is divided into three electrodes by two sine insulated gaps. The nine electrodes in each pitch are connected to their corresponding pads by bonding wires. The widths of the three electrodes A_1, A_2, and A_3 in a triplet can be expressed by

$$a_1 = \frac{p}{9} + m\sin(\theta_A),$$
$$a_2 = \frac{p}{9} + m\sin\left(\theta_A - \frac{2}{3}\pi\right),$$
$$a_3 = \frac{p}{9} + m\sin\left(\theta_A - \frac{4}{3}\pi\right), \quad (1)$$

1559-128X/15/226904-08$15/0$15.00 © 2015 Optical Society of America

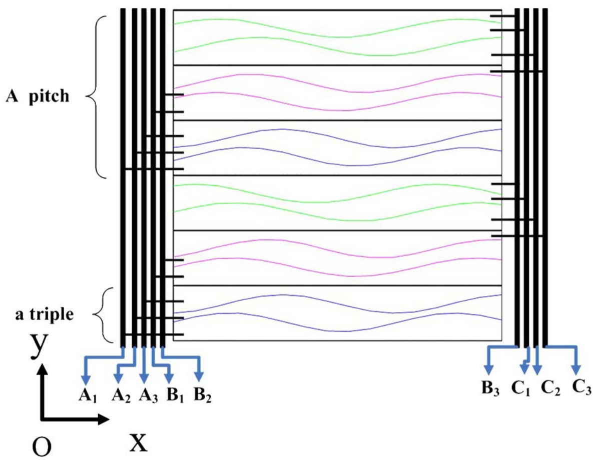

Fig. 1. Schematic of the Vernier anode with two pitches.

where p is the width of a pitch, m is the sinusoidal amplitude, and θ_A is the A triple phase along the horizontal axis.

By using MATLAB 7.5 software, a program is edited to simulate the effect of the charge cloud width on the decoding algorithm (2). In the program, the charge cloud distribution shown in Eq. (3) is used, and the charges deposited on nine electrodes are computed by the numerical integration. Therefore, the only decoding phase θ_A, θ_B, and θ_C can be calculated by Eq. (2) to determine the only corresponding decoding coordinates for any given position. Figure 2(a) shows a group of the calculated decoding positions for a group of given positions when the charge cloud covers one and two pitches, respectively. Figure 2(b) also shows a group of calculated decoding positions for a group of given positions when the charge cloud covers three, four, and six pitches. It is shown that when the charge cloud covers no fewer than three pitches, the calculated decoding positions agree well with the given ones.

B. Partition Noise of Vernier Anode

Here the triple A is taken as an instance to calculate the partition noise. Differentiating Eq. (2) and combining it with Eq. (1), one can get the following expression:

$$\delta\theta_A = \frac{2\cos\theta_A \delta Q_{A1} + \left(\sqrt{3}\sin\theta_A - \cos\theta_A\right)\delta Q_{A2} - \left(\cos\theta_A + \sqrt{3}\sin\theta_A\right)\delta Q_{A3}}{3Q_{\text{total}}\frac{m}{p}}. \tag{4}$$

For the Vernier anode, the charges deposited on all electrodes are proportional to the electrode's area covered by the charge cloud. Assuming that Q_{A1}, Q_{A2}, and Q_{A3} are the charges collected on electrodes A_1, A_2, and A_3, the triple phase θ_A can be expressed as follows:

$$\theta_A = \arctan\left[\frac{2Q_{A1} - Q_{A2} - Q_{A3}}{\sqrt{3}(Q_{A3} - Q_{A2})}\right]. \tag{2}$$

θ_B and θ_C, which represent the phase of triple B and C, can be expressed in the same form as θ_A, respectively. With θ_A, θ_B, and θ_C together, one can get the charge cloud's centroid position. Because the width of the charge cloud falling on the anode can influence the charges collected on the electrodes, it is necessary to optimize the width of the charge cloud for the Vernier anode in order to get high spatial resolution.

A. Optimal Charge Cloud's Width for Vernier Anode

So far, many models [14,15] for the charge footprint distribution have been proposed. It is shown that the real charge distribution is in the Gaussian form [6] and can be given by the following formula:

$$Q_{x,y} = \frac{Q_{\text{total}}}{\sigma\sqrt{2\pi}} \exp\left[-\frac{(x-x_0)^2 + (y-y_0)^2}{2\sigma^2}\right],$$
$$\sigma = r/2.75, \tag{3}$$

where Q_{total} is the gain of the MCP stack, (x_0, y_0) is the charge cloud's centroid coordinate on the anode, and r is the radius of the charge cloud.

Because the collected charge on the electrodes is a random partition noise process governed by statistical variations, the parameters Q_{A1}, Q_{A2}, and Q_{A3} in Eq. (4) represent the standard deviation of the charges falling on electrodes A_1, A_2, and A_3. According to the definition of the standard deviation, the electrons falling on electrode A_1 make no contribution to A_1 variance and the electrons falling on electrodes A_2 and A_3 or other electrodes make contributions to A_1 variance.

Assuming that the charges deposited on electrodes A_1, A_2, and A_3 have a Gaussian distribution as in Eq. (3), the probability density function $g(x, y)$ can be expressed as

$$g(x,y) = \frac{1}{\sigma\sqrt{2\pi}} \exp\left[-\frac{(x-x_0)^2 + (y-y_0)^2}{2\sigma^2}\right],$$
$$\sigma = r/2.75. \tag{5}$$

Based on the conclusion in Section 2.A, the charge cloud should cover no fewer than three pitches in order to obtain the exact decoding positions. So Q_{A1}, Q_{A2}, and Q_{A3} are the sums of the standard deviations of the charges falling on electrodes A_1, A_2, and A_3 for every pitch that the charge cloud covers. Q_{A1}, Q_{A2}, and Q_{A3} can be expressed as

$$\delta Q_{A1} = \sum_{i=1}^{n} \delta Q_{A1\_i},$$
$$\delta Q_{A2} = \sum_{i=1}^{n} \delta Q_{A2\_i},$$
$$\delta Q_{A3} = \sum_{i=1}^{n} \delta Q_{A3\_i}, \tag{6}$$

where Q_{A1_i}, Q_{A2_i}, and Q_{A3_i} are the standard deviations of the charges falling on electrodes A_1, A_2, and A_3 in the ith pitch.

Figure 3 gives a schematic of the charge cloud covering n pitches. In Fig. 3, the red circle represents the charge cloud, and (x_0, y_0) are the centroid coordinates of the charge cloud. A_{1_1}, A_{2_1}, A_{3_1}, A_{1_n}, A_{2_n}, and A_{3_n} represent the electrodes that are covered by the charge cloud. And y_{1_1}, y_{2_1}, y_{3_1}, y_{4_1}, y_{1_n}, y_{2_n}, y_{3_n}, and y_{4_n} represent the coordinates of the insulated gaps in the y direction.

The standard deviation of the charges collected on the electrodes A_1, A_2, and A_3 from the first pitch to the nth one shown in Fig. 3 can be expressed by the following equations:

$$
\begin{aligned}
\delta Q_{A1\_1} &= \left[Q_{\text{total}} \int_{y_0-y_{2\_1}}^{y_0-r+p} \int_{x_0-\sqrt{r^2-(y-y_0)^2}}^{x_0+\sqrt{r^2-(y-y_0)^2}} (y-y_{2\_1})^2 g(x,y)\mathrm{d}x\mathrm{d}y\right]^{1/2},\\
\delta Q_{A2\_1} &= \left\{Q_{\text{total}}\left[\begin{array}{l}\int_{y_0-y_{1\_1}}^{y_0-y_{2\_1}} \int_{x_0-\sqrt{r^2-(y-y_0)^2}}^{x_0+\sqrt{r^2-(y-y_0)^2}} (y-y_{1\_1})^2 g(x,y)\mathrm{d}x\mathrm{d}y\\ +\int_{y_0-y_{3\_1}}^{y_0-r+p} \int_{x_0-\sqrt{r^2-(y-y_0)^2}}^{x_0+\sqrt{r^2-(y-y_0)^2}} (y-y_{3\_1})^2 g(x,y)\mathrm{d}x\mathrm{d}y\end{array}\right]\right\}^{1/2},\\
\delta Q_{A3\_1} &= \left\{Q_{\text{total}}\left[\begin{array}{l}\int_{y_0-y_{1\_1}}^{y_0-y_{3\_1}} \int_{x_0-\sqrt{r^2-(y-y_0)^2}}^{x_0+\sqrt{r^2-(y-y_0)^2}} (y-y_{3\_1})^2 g(x,y)\mathrm{d}x\mathrm{d}y\\ +\int_{y_0-y_{4\_1}}^{y_0-r+p} \int_{x_0-\sqrt{r^2-(y-y_0)^2}}^{x_0+\sqrt{r^2-(y-y_0)^2}} (y-y_{4\_1})^2 g(x,y)\mathrm{d}x\mathrm{d}y\end{array}\right]\right\}^{1/2},\\
&\vdots \quad \vdots \quad \vdots\\
\delta Q_{A1\_n} &= \left[Q_{\text{total}} \int_{y_0+r-y_{2\_n}}^{y_0+r} \int_{x_0-\sqrt{r^2-(y-y_0)^2}}^{x_0+\sqrt{r^2-(y-y_0)^2}} (y-y_{2\_n})^2 g(x,y)\mathrm{d}x\mathrm{d}y\right]^{1/2},\\
\delta Q_{A2\_n} &= \left\{Q_{\text{total}}\left[\begin{array}{l}\int_{y_0+r-y_{1\_n}}^{y_0+r-y_{2\_n}} \int_{x_0-\sqrt{r^2-(y-y_0)^2}}^{x_0+\sqrt{r^2-(y-y_0)^2}} (y-y_{1\_n})^2 g(x,y)\mathrm{d}x\mathrm{d}y\\ +\int_{y_0+r-y_{3\_n}}^{y_0+r} \int_{x_0-\sqrt{r^2-(y-y_0)^2}}^{x_0+\sqrt{r^2-(y-y_0)^2}} (y-y_{3\_n})^2 g(x,y)\mathrm{d}x\mathrm{d}y\end{array}\right]\right\}^{1/2},\\
\delta Q_{A3\_n} &= \left\{Q_{\text{total}}\left[\begin{array}{l}\int_{y_0+r-y_{1\_n}}^{y_0+r-y_{3\_n}} \int_{x_0-\sqrt{r^2-(y-y_0)^2}}^{x_0+\sqrt{r^2-(y-y_0)^2}} (y-y_{3\_n})^2 g(x,y)\mathrm{d}x\mathrm{d}y\\ +\int_{y_0+r-y_{4\_n}}^{y_0+r} \int_{x_0-\sqrt{r^2-(y-y_0)^2}}^{x_0+\sqrt{r^2-(y-y_0)^2}} (y-y_{4\_n})^2 g(x,y)\mathrm{d}x\mathrm{d}y\end{array}\right]\right\}^{1/2}.
\end{aligned}
\tag{7}
$$

Combining Eqs. (4)–(6) with Eq. (7), one can get the phase change due to the partition noise:

$$\delta\theta_A = \frac{p}{3m}\frac{1}{Q_{\text{total}}} f(\theta_A), \tag{8}$$

where

$$
\begin{aligned}
f(\theta_A) = {} & 2\cos\theta_A \delta Q_{A1} + \left(\sqrt{3}\sin\theta_A - \cos\theta_A\right)\delta Q_{A2}\\
& - \left(\cos\theta_A + \sqrt{3}\sin\theta_A\right)\delta Q_{A3}.
\end{aligned}
\tag{9}
$$

Combining Eqs. (7), (8), and (9), one can see that the partition noise of a triple phase is determined by the gain of the MCP stack Q_{total}, the ratio of p to m, and the value of $f(\theta_A)$, where $f(\theta_A)$ is related to the anode's structure and the charge cloud's radius.

Figure 4(a) shows $\delta\theta_A$ as a function of θ_A for different p/m when $p = 0.891$ mm, b for different p with $p/m = 18$, c for different charge cloud's width, and d for different Q_{total} when $p = 0.891$ mm, $p/m = 18$. It can be seen that the value of $\delta\theta_A$ is dependent on the pitch width, the ratio of p to m, the gain of MCP stacks, and the charge cloud's width.

3. ELECTRONIC NOISE OF THE VERNIER ANODE

The electronic noise from CSA is the other factor affecting the spatial resolution of the charge divided anode, which influences the event decoding position. The electron noise level is mainly determined by the capacitive load, which corresponds to the inter-electrode capacitance of the anode [9]. It can be represented by

$$N = N_0 + N_u C, \tag{10}$$

where N_0 is the equivalent noise charge (ENC) of a CSA with zero capacitive loading, N_u is its ENC slope (the root mean square charge per unit capacitance), and C is the capacitive load. In the following, a method to calculate the inter-electrode capacitance and the influence of the electronic noise on event decoding position will be given.

A. Method to Calculate the Inter-Electrode Capacitance

The Vernier anode is manufactured by using a laser micromachining method to ablate the metal film (Cu or Al) with a thickness of 0.002 mm sputtered on an insulating substrate (quartz or ceramics). Thus there is capacitance between the neighboring electrodes due to the insulation gap. A section of the two neighboring electrodes A_1 and A_2 in a triplet is shown

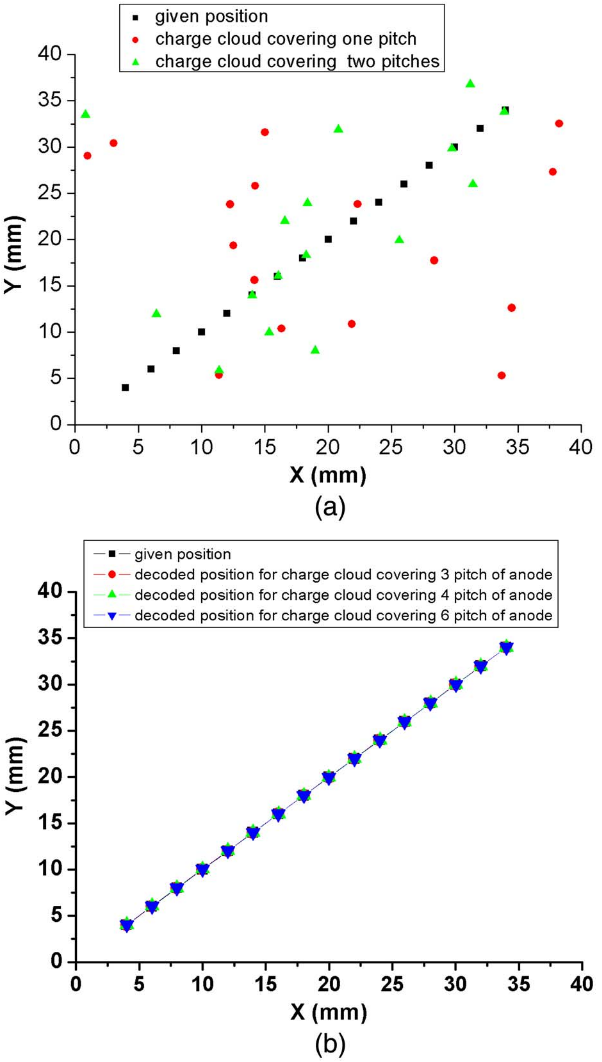

Fig. 2. Calculated decoding position when charge cloud covers (a) one to two pitches and (b) no fewer than three pitches for a group of given positions.

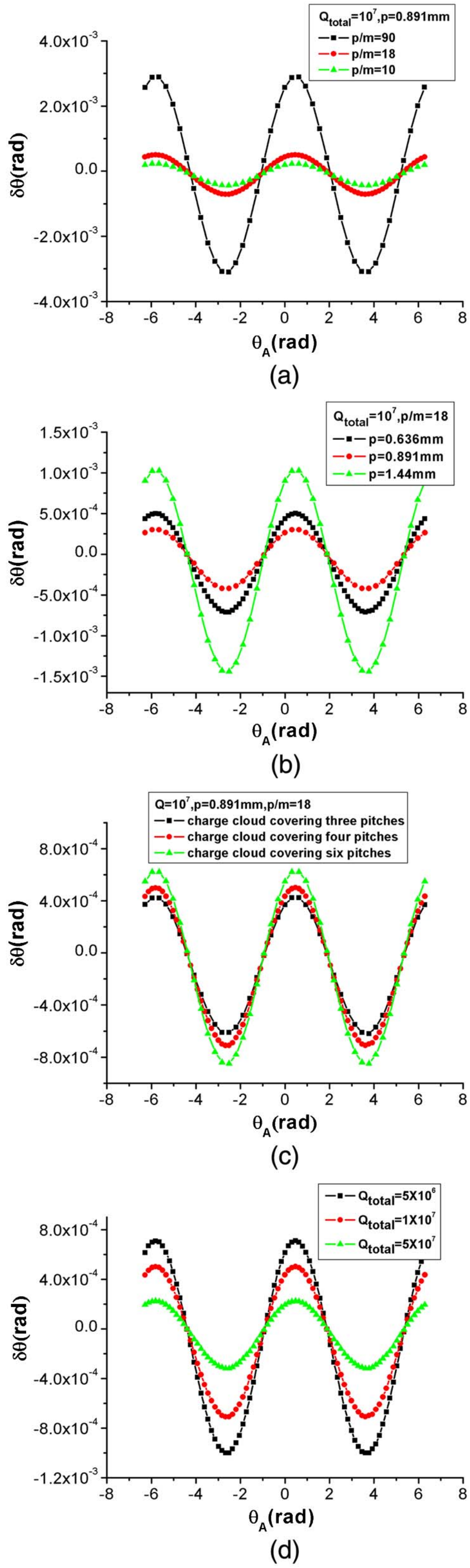

Fig. 4. Value of $\delta\theta_A$ as a function of A triple phase with different ratio of p to m for $p = 0.891$ mm in (a), with different p for $p/m = 18$ in (b), with different charge cloud width for $p = 0.891$ mm and $p/m = 18$ in (c), and with different gain of MCP stacks for $p = 0.891$ mm and $p/m = 18$ in (d).

in Fig. 5, where g is the width of the insulation gap, and a_1 and a_2 are the widths of electrodes A_1 and A_2, respectively. A Vernier anode with n periods has n triplets, and all of them are connected by bonding wires. Hence the total inter-electrode capacitance between electrodes A_1 and A_2 is n times the capacitance between electrodes A_1 and A_2 in a triplet, which is shown in Fig. 5.

Normally, compared to the electrode width and the insulation gap width, the thickness of the metal film can be ignored.

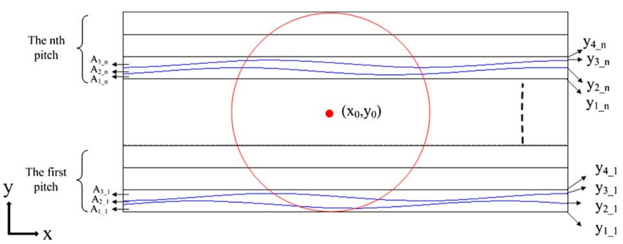

Fig. 3. Standard deviation for triple A.

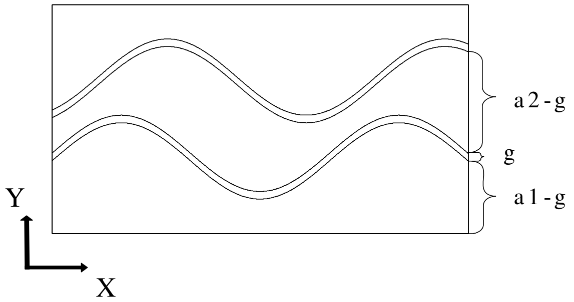

Fig. 5. Section of the neighboring electrodes, A_1 and A_2.

By using the Schwarz–Christoffel transformation [16], the unit length of the inter-electrode capacitance between electrodes A_1 and A_2 in a triplet can be obtained as follows:

$$C_0 = 2\varepsilon_{\text{eff}} K(k_c')/K(k_c), \tag{11}$$

where K is the complete elliptic integral of the first kind. Parameters k_c and k_c' are defined by

$$k_c = \left[\frac{(a_1 + a_2 - g)g}{(a_1 + a_2 - 2g)a_2}\right]^{1/2}, \tag{12}$$

$$k_c' = \sqrt{1 - k_c^2}, \tag{13}$$

where ε_{eff} is the effective permittivity and can be expressed by

$$\varepsilon_{\text{eff}} = \varepsilon_0(1 + \varepsilon)/2, \tag{14}$$

where ε is the relative permittivity of the substrate.

The total capacitance between the neighboring electrodes A_1 and A_2 can be given by

$$C = 2\varepsilon_{\text{eff}} n \int_0^L K(k_c')/K(k_c)\mathrm{d}l, \tag{15}$$

where L is the length of the Vernier anode along the x direction.

Figure 6(a) shows the total inter-electrode capacitance C varying with the ratio of p to m for a Vernier anode with parameters $L = 38.313$ mm, $n = 43$, $\varepsilon = 3.6$, and $g = 0.025$ mm. Figure 6(b) shows the relationship between the insulation gap g and the capacitance C. As can be seen, the capacitance is insensitive to the value of p/m but sensitive to the gap width and the pitch width. The larger the gap width, the smaller the total inter-electrode capacitance and the charge effective area. The smaller the pitch width, the smaller the capacitance. However, the manufacturing of the anode becomes more challenging. The use of a substrate with low permittivity such as quartz and the reduction of the period number also help to reduce the inter-electrode capacitance effectively.

By using Eq. (15), one can also get the capacitance value between the other two neighboring electrodes. To prove the validity of the above method, a Vernier anode was fabricated by using a femtosecond pulse laser to inscribe the 0.002 mm thick Cu film on a quartz substrate, which is shown in Fig. 7. The parameters of the fabricated anode are shown in Table 1. Table 2 shows the measured inter-electrode capacitances and the calculated values. The calculated values in Table 2 contain the capacitance between bonding wire pads, which is about 2.17 pF, and the influence of bonding wires is ignored. The average deviation between the calculated and measured values is less than 6%, which is much smaller than that of 17% by employing the previously reported method, which only considers the strips with equal width in WSA [12].

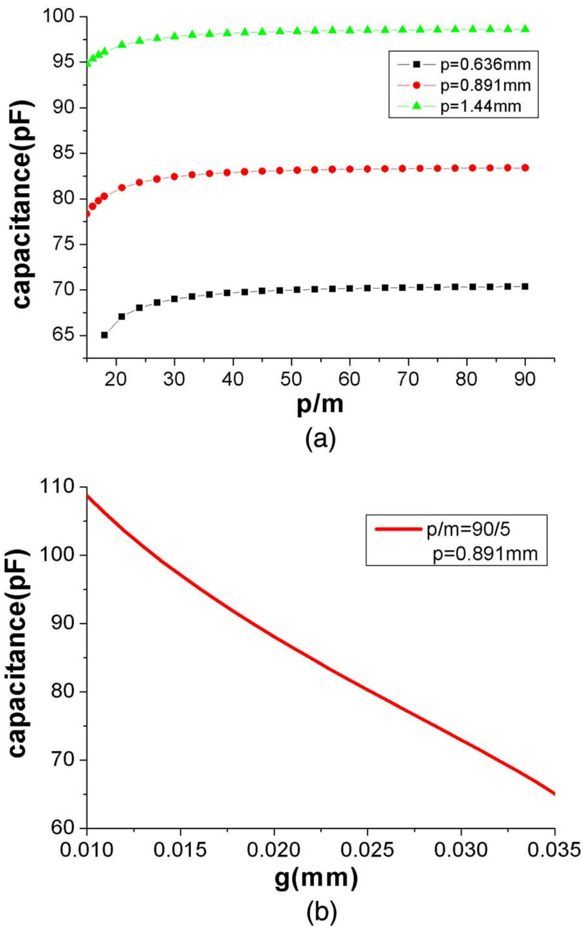

Fig. 6. Calculated inter-electrode capacitance between electrodes A_1 and A_2 (a) with different pitch width and (b) with different insulation gap.

B. Electronic Noise

Assuming all the ENCs of electrodes A_1–A_3 from their inter-electrode capacitances are N_{A1}, N_{A2}, and N_{A3}, the total

Fig. 7. Photograph of a 38 mm × 38 mm Vernier anode made in copper film on a quartz substrate.

Table 1. Design Parameters of the Vernier Anode

Width of period (p)	0.891 mm
Number of period (n)	43
Length in x direction (L)	38.313 mm
Width of insulation gap (g)	0.025 mm
Sinusoidal amplitude (m)	0.05 mm
Substrate relative permittivity (ε)	3.6
Wavelength in x direction (λ_x)	5.47 mm

Table 2. Comparison of the Calculated Values with the Measured Ones for All the Inter-Electrode Capacitances

Electrode	Calculated (pF)	Measured Value (pF)
A_1, A_2	84.8	85.8
A_2, A_3	82.6	87.2
A_3, B_1	84.9	88.8
B_1, B_2	84.7	88.3
B_2, B_3	80.0	84.2
B_3, C_1	84.8	89.1
C_1, C_2	84.7	86.8
C_2, C_3	82.7	87.8
C_3, A_1	81.8	84.6

charges fed to the CSA for the three electrodes are $Q_{A1} + N_{A1}$, $Q_{A2} + N_{A2}$, and $Q_{A3} + N_{A3}$. Then based on Eq. (2), one can get the triple phase θ_{A1} of the charge cloud's centroid position due to electronic noise as follows:

$$\tan\theta_{A1} = \frac{2(Q_{A1}+N_{A1}) - (Q_{A2}+N_{A2}) - (Q_{A3}+N_{A3})}{\sqrt{3}(Q_{A3}+N_{A3}-Q_{A2}-N_{A2})}. \tag{16}$$

The ideal triple phase θ_{A0} of the charge cloud's centroid position can be represented by

$$\tan\theta_{A0} = \frac{2Q_{A1} - Q_{A2} - Q_{A3}}{\sqrt{3}(Q_{A3} - Q_{A2})}. \tag{17}$$

Then the deviation of triple phase θ_{A1} to θ_{A0} can be given by

$$\begin{aligned} d\theta_e \approx \tan(d\theta_e) &= \frac{\tan\theta_{A1} - \tan\theta_{A0}}{1 + \tan\theta_{A1}\tan\theta_{A0}} \\ &\approx \frac{p/m}{3Q_{\text{total}}}[(2N_{A1} - N_{A2} - N_{A3})\cos\theta_A \\ &\quad - \sqrt{3}(N_{A3} - N_{A2})\sin\theta_A]. \end{aligned} \tag{18}$$

Combining Eq. (18) with Eqs. (1) and (10), one can get

$$\begin{aligned} d\theta_e \approx &\frac{p/m}{3Q_{\text{total}}}N_u[(2C_{C3\text{-}A1} + C_{A1\text{-}A2} - 2C_{A2\_A3} - C_{A3\_B1})\cos\theta_A \\ &- \sqrt{3}(C_{A3\_B1} - C_{A1\_A2})\sin\theta_A]. \end{aligned} \tag{19}$$

Here C_{C3_A1}, C_{A1_A2}, C_{A2_A3}, and C_{A3_B1} represent the capacitance between C_3, A_1, A_2, A_3, and B_1, respectively.

Figure 8 gives the deviation of the triple phase for different p/m, MCP gain, and ENC slope.

According to Eq. (19) and Fig. 8, one can see that the deviation of triple phase $d\theta_e$ is proportional to the value of p/m and the ENC slope, and is inversely proportional to the gain of MCP stacks. At the same time, it is relative to the difference of inter-electrode capacitances.

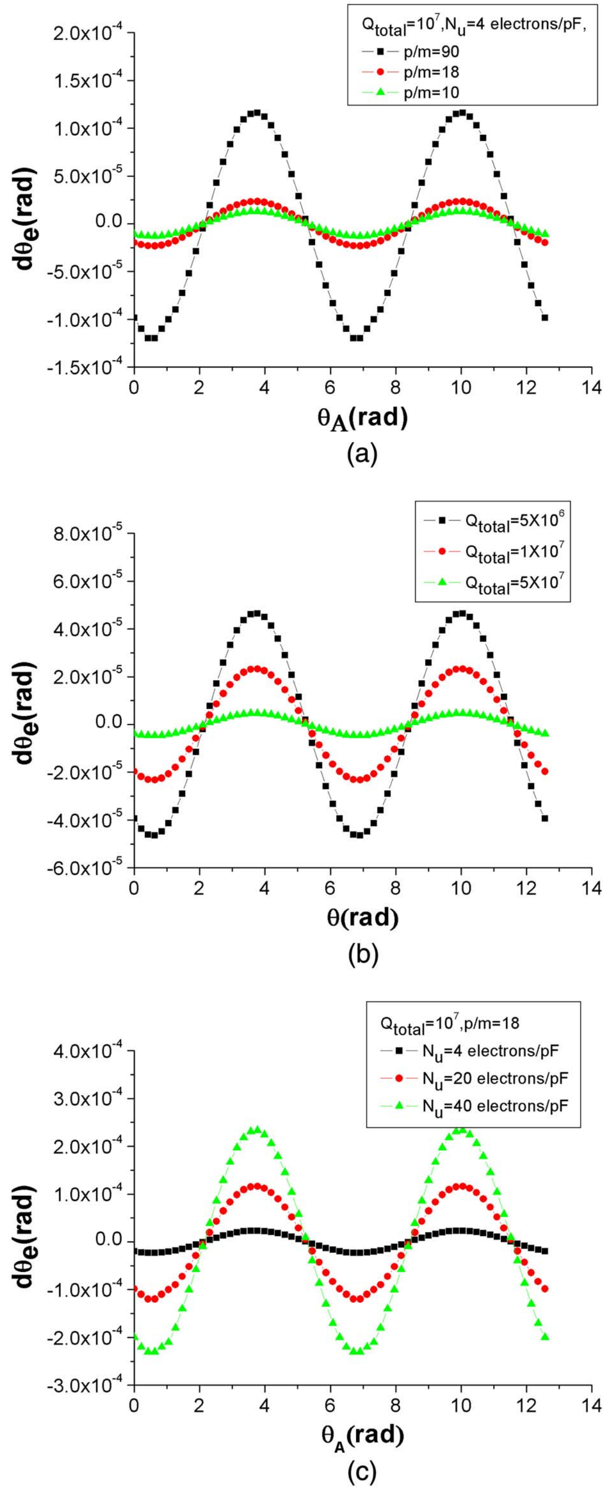

Fig. 8. Deviation of triple phase (a) for different p/m, (b) for different MCP gain, and (c) for different ENC slope.

4. SPATIAL RESOLUTION OF THE VERNIER ANODE

Generally, the factors that mainly determine the Vernier anode resolution include the partition noise and the electron noise. The position coordinates [17] of the charge cloud's centroid can be expressed as

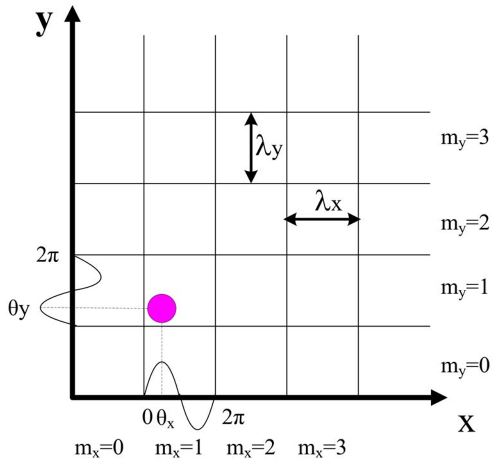

Fig. 9. Sketch of event position in x–y plane.

$$x = \lambda_x \frac{\theta_x}{2\pi} + m_x \lambda_x,$$
$$y = \lambda_y \frac{\theta_y}{2\pi} + m_y \lambda_y. \quad (20)$$

Here λ_x and λ_y are the resultant phases of x and y wavelength, respectively, θ_x and θ_y are the resultant phases corresponding to a wavelength cycle, and m_x and m_y are the whole numbers of wavelength corresponding to the x and y positions, respectively. Figure 9 shows a sketch of the event coordinates in the x–y plane.

The relationship between θ_x and m_x, θ_y and m_y can be expressed by

$$2\pi m_x + \theta_x = \theta_A + \theta_B,$$
$$2\pi m_y + \theta_y = \theta_B + \theta_C. \quad (21)$$

Here θ_A, θ_B, and θ_C are the phases of triplets A, B, and C, respectively.

The extremely tiny change of θ_A, θ_B, and θ_C strongly influences θ_x and θ_y but has nearly no effect on m_x and m_y. Therefore m_x and m_y can be considered as constants in this case. By differentiating Eq. (21), one can get the following expressions:

$$dx = \frac{\lambda_x}{2\pi} d\theta_x = \frac{\lambda_x}{2\pi}(d\theta_A + d\theta_B),$$
$$dy = \frac{\lambda_y}{2\pi} d\theta_y = \frac{\lambda_y}{2\pi}(d\theta_B + d\theta_C). \quad (22)$$

According to Eqs. (8) and (19), one can get the FWHM resolution due to partition noise and electronic noise in the x–y plane, respectively. The total resolution of the Vernier anode in the x–y plane can be expressed as

$$R = \sqrt{R(PN)^2 + R(EN)^2}. \quad (23)$$

5. OPTIMIZATION OF THE VERNIER ANODE AND DETECTOR CONFIGURATION

We have developed models to investigate the essential factors influencing the spatial resolution of the Vernier anode. The optimal anode configuration and detector operating parameters are predicted as follows in order to achieve better spatial resolution.

A. Maximize the gain of MCP stacks.

The partition noise is inversely proportional to the value of $\sqrt{Q_{\text{total}}}$, and the electronic noise is inversely proportional to the value of Q_{total}. Increase in the gain of MCP stacks can strongly improve the spatial resolution.

B. Minimize the pitch.

Both the partition noise and the electron noise are proportional to the pitch width. At the same time, decrease in the pitch can reduce the capacitance of the Vernier anode. Hence the width of the pitch should be decreased as much as possible.

Because there are nine insulted gaps included in a pitch, mechanical errors in the pattern fabrication increase proportionately as the pitch is reduced. And the wire bonding techniques that can make electrical interconnections limit the average electrode width to ~0.075 mm.

C. Maximize the ratio of the pitch to the electrode sinusoidal amplitude.

Similarly, the partition noise, the electron noise, and the capacitance of the Vernier anode are proportional to the ratio of the pitch to the electrode sinusoidal. Hence the ratio of p to m should be decreased. When the pitch width is fixed, an increase in the electrode sinusoidal amplitude can maximize the ratio. But the minimum electrode width between two insulted gaps should not be smaller than 0.03 mm in order to prevent the connection between the neighboring electrodes.

D. Generate suitable charge cloud width.

Increasing the charge cloud width can increase the partition noise. But a too-small charge cloud width can lead to severe imaging distortion. The simulation of the charge cloud width on the decoding algorithm of the Vernier anode gives the smallest charge cloud width, no fewer than three pitches of the Vernier anode.

6. CONCLUSION

In summary, this paper presents a theoretical method to determine the partition noise, the electronic noise, and the inter-electrode capacitance of the Vernier anode. It is apparent that both the partition noise and the electronic noise are related to the MCP stack's gain, the pitch width, and the ratio of the pitch width to the electrode sinusoidal amplitude. Increasing the MCP stack's gain and the p/m ratio can raise both the partition noise and the electronic noise. Meanwhile, the partition noise is related to the charge cloud's width. The larger the charge cloud, the greater the partition noise. Based on the simulation of the charge cloud width on the decoding algorithm of the Vernier anode, the optimal charge cloud's width should be three pitches of the Vernier anode to avoid modulation effects for smaller width and more partition noise for larger width. Because of the structure and the decoding method of the Vernier anode, the effect of electronic noise on the resolution mainly depends on the differential of electronic noise among three electrodes in a triple. The calculated inter-electrode capacitance by using the Schwarz–Christoffel transformation is in reasonable agreement with the experimental one. Low capacitance can be achieved by reducing the pitch width and increasing the inter-electrode width. These results are preferable for one to design the Vernier anode.

Funding. National Natural Science Foundation of China (61275152, 61475154).

REFERENCES

1. K. Werner and N. Kappelmann, "New detector developments for future UV space missions," in *40th COSPAR Scientific Assembly* (2014).
2. K. Werner, J. Barnstedt, W. Gringel, N. Kappelmann, H. Becker-Ross, S. Florek, R. Graue, D. Kampf, A. Reutlinger, C. Neumann, B. Shustov, A. Moisheev, and E. Skripunove, "HIRDES—the high-resolution double-echelle spectrograph for the World Space Observatory Ultraviolet (WSO/UV)," Adv. Space Res. **41**, 1992–1997 (2008).
3. D. C. Slater, J. Timothy, and J. S. Morgan, "Imaging MAMA detector systems," Proc. SPIE **1243**, 124348 (1990).
4. G. Da Costa, F. Vurpillot, A. Bostel, M. Bouet, and B. Deconihout, "Design of a delay-line position-sensitive detector with improved performance," Rev. Sci. Instrum. **76**, 013304 (2005).
5. O. H. W. Siegmund, "High-performance microchannel plate detectors for UV/visible astronomy," Nucl. Instrum. Methods Phys. Res. A **525**, 12–16 (2004).
6. O. H. W. Siegmund, A. S. Tremsin, and R. Abiad, "Cross-strip anodes for microchannel plate detectors," Proc. SPIE **4498**, 131–140 (2001).
7. J. S. Lapington, "A comparison of readout techniques for high-resolution imaging with microchannel plate detectors," Nucl. Instrum. Methods Phys. Res. A **525**, 361–365 (2004).
8. J. S. Lapington and B. Sanderson, "Microchannel plate limited resolution with the Vernier anode," Proc. SPIE **4139**, 242–246 (2000).
9. J. R. Howorth and J. R. Powell, "Imaging photon detectors," Proc. SPIE **1243**, 124356 (1990).
10. O. H. W. Siegmund, S. Clothier, J. Thornton, J. Lemen, R. Harper, I. M. Mason, and J. L. Vulhane, "Application of the wedge and strip anode to position sensing with microchannel plates and proportional counters," IEEE Trans. Nucl. Sci. **30**, 503–507 (1983).
11. C. Martin, P. Jelinsky, M. Lampton, R. F. Malina, and H. O. Anger, "Wedge and strip anodes for centroid finding position sensitive photon and particle," Rev. Sci. Instrum. **52**, 1067–1074 (1981).
12. J. Thornton, "The inter-electrode capacitance of wedge and strip position sensing elements," Nucl. Instrum. Methods Phys. Res. A **269**, 226–229 (1988).
13. J. S. Lapington and H. E. Schwarz, "The design and manufacture of wedge and strip anodes," IEEE Trans. Nucl. Sci. **33**, 288–292 (1986).
14. A. S. Tremsin, J. V. Vallerga, O. H. W. Siegmund, and J. S. Hul, "Centroiding algorithms and spatial resolution of photon counting detectors with cross strip anodes," Proc. SPIE **5164**, 113–124 (2003).
15. A. Smith, R. Kessel, J. S. Lapington, and D. M. Walton, "Modulation effects in wedge and strip anodes," Rev. Sci. Instrum. **60**, 3509–3518 (1989).
16. C. Ruan, L. Heng, and H. N. Liang, "Double-layer substrate asymmetrical coplanar lines," J. China Inst. Commun. **21**, 2186–2190 (2000).
17. H. Yang, B. S. Zhao, Q. R. Yan, Y. A. Liu, and H. J. Hu, "Decoding algorithm of single photon counting imager based on two-dimensional Vernier anodes," Sci. China Phys. Mech. Astron. **54**, 1943–1947 (2011).